ORIGINAL RESEARCH

A SPECT/NIR Fluorescence Dual-Modality Imaging Agent Composed of Drugs and Hospital Available Isotope for Preoperative Sentinel Lymph Node Mapping and Intraoperative Biopsy

Ming Zhou[1,2,*], Peng Liu[1,2,*], Xiaoqin Yin[1], Caiting Deng[3,4], Yi Xiao[1], Meng Lei[1], Shuo Hu[1], Feifei An[3], Min Zhao[1,5,6]

[1]Department of Nuclear Medicine, Xiangya Hospital, Central South University, Changsha, People's Republic of China; [2]Key Laboratory of Biological, Nanotechnology of National Health Commission, Xiangya Hospital, Central South University, Changsha, People's Republic of China; [3]School of Public Health, Health Science Center, Xi'an Jiaotong University, Xi'an, People's Republic of China; [4]Institute of Medical Engineering, Department of Biophysics, School of Basic Medical Science, Health Science Center, Xi'an Jiaotong University, Xi'an, People's Republic of China; [5]Department of Nuclear Medicine, Third Xiangya Hospital, Central South University, Changsha, People's Republic of China; [6]National Clinical Research Center of Geriatric Disorders, Xiangya Hospital, Central South University, Changsha, People's Republic of China

*These authors contributed equally to this work

Correspondence: Min Zhao; Feifei An, Email mzhao1981@csu.edu.cn; anfeifei@xjtu.edu.cn

Background: Sentinel lymph node (SLN) mapping-guided biopsy is crucial for cancer staging and treatment. Optical/nuclide dual-modality imaging agents for mapping SLN are ideal for preoperative planning and intraoperative biopsy, which are enabled by penetration-depth unlimited nuclide imaging and dynamic real-time optical imaging, respectively. However, commonly reported dual-modality imaging agents are composed of novel but safety-unproven materials, making their quick clinical translation challenging. Herein, we report a novel nanoparticle composed of facile hospital-available drugs and isotope for single-photon emission computed tomography (SPECT)/near-infrared (NIR) fluorescence imaging to detect SLNs.
Methods: Indocyanine green-human serum albumin (ICG-HSA) nanoparticles (NPs) were synthesized by ICG-induced HSA self-assembly and further ^{99m}Tc-labeling via a one-step, facile hospital-available method. After injecting ^{99m}Tc-ICG-HSA into the rats' forepaw pads, the rats' draining axillary lymph nodes were visualized by preoperative mapping with SPECT/CT and intraoperative biopsy with NIR fluorescence. The axillary lymph nodes of rats were identified by pathology and fluorescent staining after execution. Additionally, its toxicity testing and comparison with ^{99m}Tc-sulfur colloid imaging were also explored.
Results: The study reported a self-assembled ^{99m}Tc-ICG-HSA with a high radiochemical yield (85.6 ± 3.8%). Compared with conventional ^{99m}Tc-sulfur colloid, ^{99m}Tc-ICG-HSA NPs showed faster SLN identification, higher renal clearance, and lower hepatic retention. Furthermore, NIRF imaging allowed for the accurate visualization of the SLN and guided SLN biopsy intraoperatively. Notably, the ^{99m}Tc-ICG-HSA NPs were composed of hospital-available drugs and isotope, which are safe for acute toxicity evaluation by a certified institute.
**Conclusion:** The proposed ^{99m}Tc-ICG-HSA NPs are safe and capable of noninvasive SLN identification and biopsy guidance with multi-modal imaging strategies and could be a promising tool for clinically assisted SLN biopsy.
Keywords: image-guided surgery, indocyanine green, albumin, fluorescence imaging, near-infrared, single-photon emission computed tomography

Introduction

Cancer is currently the leading cause of premature death and the only cure for early-stage cancer is to remove as much of the primary tumor and regional lymph node (LN) as possible, along with the margins of normal tissue.[1–3] Previous studies have shown that prophylactic extended lymphadenectomy has no apparent survival benefit for cancer patients, and this approach is associated with a higher risk of complications such as lymphedema, dysfunction, and pain that

Graphical Abstract
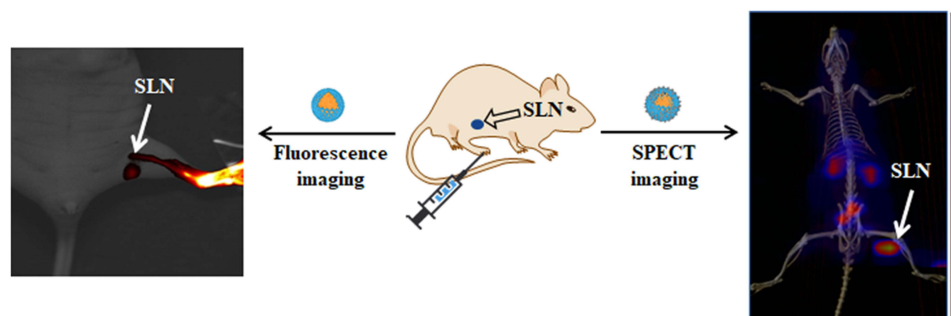
reduce quality of life.[4–8] The sentinel lymph node (SLN) is the first site that receives lymphatic drainage from the primary tumor site.[9] In any type of malignant tumor, the most accurate LN staging methods include SLN mapping, surgical resection, and pathological examination.[10,11] Therefore, SLN biopsy (SLNB) has been recognized as an important technique in various cancer surgeries.[12–14]

At present, the primary clinical methods for accurate SLN imaging and localization are optical imaging, naked eye observation with blue dye or near-infrared fluorescence (NIRF) imaging with indocyanine green (ICG), and radioisotope imaging.[15,16] However, optical imaging has poor tissue penetration and sensitivity when the cancer and the corresponding SLN are located in internal organs.[17,18] Meanwhile, these agents travel fast through the SLN to second-tier nodes, resulting in false-negative results and relatively low sensitivity and specificity.[19,20] On the other hand, ^{99m}Tc-labeled radiocolloid exhibits excellent tissue depth penetration and high specificity for intraoperative SLN mapping, making it ideal for preoperative identification of the anatomical location of SLNs.[21,22] However, the typical radiotracer injection sites (such as the floor of the mouth) in tumor lesions are adjacent to SLN and may result in the phenomena of "shine through", thus leading to false-negative identification.[23–25] Given their own strengths and pitfalls, single-photon emission computerized tomography (SPECT) and near-infrared fluorescence (NIRF) dual-modality imaging agent may complement each other for optimized properties and applications.[26,27] However, these agents contain novel materials that are not clinically available, which makes their rapid clinical application difficult.

In this study, a novel dual-modality SLN imaging agent, ^{99m}Tc-ICG-HSA nanoparticles (^{99m}Tc-ICG-HSA NPs), was synthesized by spontaneous assembly of HSA and ICG, and further radiolabeling with Tc-99m via a one-step, facile method with high radiochemical yields (85.6 ± 3.8%) (Scheme 1). More importantly, the reported ^{99m}Tc-ICG-HSA NPs were composed of totally hospital available drugs and isotopes. The safety of prepared methods and drugs ensured ^{99m}Tc-ICG-HSA NPs to be safe in an acute toxicity evaluation by a professional institute. The results exhibited that ^{99m}Tc-ICG-HSA NPs are superior to conventional ^{99m}Tc-sulfur colloid in faster SLN identification, higher renal clearance, and lower hepatic retention. Further NIRF imaging allowed accurate visualization of SLN and guided SLN biopsy intraoperatively.

Materials and Methods
General
All chemicals and solvents were purchased commercially and used without further purification. ^{99m}TcO$_4^-$ was purchased from HTA Co. Ltd. (Changsha, China). HSA, ICG, and FITC were purchased from MERYER (Shanghai, China). Ultrafiltration tubes were purchased from Merck (New Jersey, USA). Radioanalysis was performed using a radiothin-layer chromatography scanner (Eckert@Ziegler, USA). Radioactivity was detected using a WIZARD 2480 γ-counter (PerkinElmer). SPECT imaging was performed using a clinical SPECT/CT system (Precedence 16; Philips, The Netherlands). CT and SPECT projections were reconstructed and analyzed using an EBW workstation (Philips, The Netherlands).
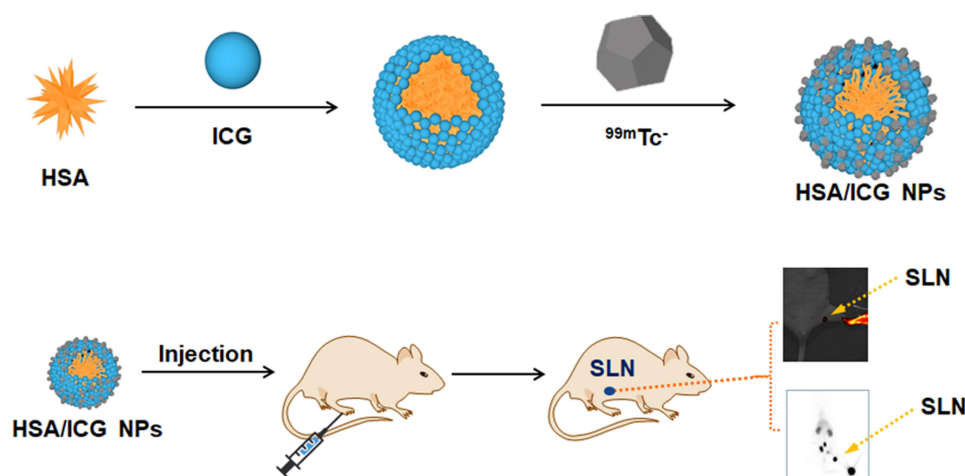
Scheme 1 Self-assembly and radiolabeling of ICG-HSA NPs and their applications for SLN Imaging.

Synthesis and Characterization of ^{99m}Tc-ICG-HSA NPs

The NPs were synthesized according to our previous report.[28] For simplicity, HSA and ICG were dissolved in double-distilled water (ddH$_2$O) at a weight ratio of 4 to 1 and then the mixture solution was stirred overnight in the dark. The mixture was transferred to a dialysis bag (cutoff = 14 kDa) and dialyzed in ddH$_2$O for 24 h to remove the unbound small molecules. The mixture solution was then filtered with a 0.22 μm filter membrane to remove oversized nanoparticles, making the obtained nanoparticles more uniform in particle size. The resulting solution was named ICG-HSA NPs and was lyophilized into a powder. ICG-HSA NPs and HSA were characterized using dynamic light scattering (DLS) (Zetasizer Nano ZSE, Malvern panalytical, China). ICG-HSA NPs were further characterized using transmission electron microscopy (TEM) (H-7650, Hitachi Hi-Tech, Japan). The absorption and fluorescence emission spectra of free ICG and ICG-HSA NPs were measured using a UV-Vis-NIR spectrophotometer (759S UV-Vis Spectrophotometer, Lengguang Technology, China, Shanghai) and a fluorescence spectrophotometer (Hitachi F-4700, Hitachi High-Technologies, Japan).

ICG-HSA NPs (2.3 mg) was dissolved in ddH$_2$O (1 mL), then added 10 μL of 1 mg/mL SnCl$_2$ solution and 0.5 mL of ^{99m}TcO$_4^-$ (758.5 MBq) solution. After shaking, the reaction was allowed to proceed at room temperature for 30 min. Taking 0.5 mL solution of the reaction system, it was placed into an ultrafiltration tube (cutoff = 100 kDa) for centrifugation (8000 rpm, 15 min). After washing with deionized water (0.5 mL), the purified ^{99m}Tc-ICG-HSA was obtained. ^{99m}Tc-ICG-HSA solution was diluted to 5 mL and slowly passed through a 0.22 μm filter. The activity of the final filtrate and the residual activity in the filter were measured. The final radiochemical yield of ^{99m}Tc-ICG-HSA NPs was calculated to be $85.6 \pm 3.8\%$. An appropriate amount of ^{99m}Tc-ICG-HSA NPs was used for thin-layer chromatography (TLC) to determine the radiochemical purity of the drug. Results showed that the radiochemical purity of ^{99m}Tc-ICG-HSA NPs in human serum solution was $98.3 \pm 1.2\%$, $95.1 \pm 1.7\%$, and $91.2 \pm 2.1\%$ at 1, 6, and 12 h, respectively (Figure S1).

Preparation of FITC Labeled ICG-HSA NPs

A DMSO solution of FITC (0.5 mL, 1 mg/mL) was mixed with the HSA solution (20 mL, 5 mg/mL, 1x PBS buffer, pH 7.4) and stirred overnight. The solution was then dialyzed against ultrapure water (18.2 MΩ), and fresh water was changed every 4 h. After 24 h, the solution was frozen and lyophilized into a dried FITC-labeled HSA powder. FITC-HSA and ICG were dissolved, mixed, and stirred overnight in distilled water. The solution was then placed in a dialysis bag (30 kDa) and dialyzed for 24 h to remove the free ICG. Filtering (0.22 μm) was applied to remove precipitated macromolecules before obtaining the final FITC-ICG-HSA NPs aqueous solution.

In vivo Toxicity Evaluation of the ICG-HSA NPs

According to the toxicological data, the acute toxicity of ICG was LD50 50–80 mg/kg (intravenously).[29] For in vivo toxicity evaluation, the prepared ICG-HSA NPs were sent to a certified institute (Hunan Anshengmei Pharmaceutical Research

Institute Co., Ltd.) for professional evaluation. In the evaluation, the ICR (Institute of Cancer Research) mice (n = 40, 17.9–19.7 g, half male and half female) were randomly divided into two groups (n = 20, half male and half female): the normal control group and the ICG-HSA NPs administration group. The mice were fasted for at least 12 h before the experiment. The ICG-HSA NPs administration group was intravenously injected with ICG-HSA NPs at an almost double dose of the LD50 of ICG (120 mg/kg), and PBS (10 mL/kg) was administered to the control group. After administration, the characteristics of poisoning symptoms, occurrence and recovery time of the poisoning reaction, and death of mice were observed and recorded in detail within 0–4 h. Meanwhile, the body weights and deaths of the mice were recorded on days 4, 7, 10, and 14th days.

Dynamic Fluorescence Images of ICG-HSA NPs in Mice SLN and Slice Examination of SLN

ICG-HSA NPs (10 μg/50 μL) were injected subcutaneously into the left footpad of BAL b/c mice and imaged immediately using a small-animal real-time imaging system (VISQUE InVivo Smart-LF, BIOTIMES, China). One image was taken every minute for 60 min to observe the dynamic targeting and accumulation of ICG-HSA NPs in the mouse SLN. After dynamic imaging, SLN of the mice were resected and collected under fluorescence imaging guidance. SLNs were sliced and stained with hematoxylin and eosin (H&E) for histological examination.

Fluorescence Imaging of ICG-HSA NPs Guiding SLN Resection Surgery and Slice Examination

ICG-HSA NPs (100 μg/50 μL) were injected subcutaneously into the right footpads of Sprague Dawley rats (n=5). Thirty minutes later, SLN resection surgery was performed under the guidance of a Fluorescence Imaging System device (DPM-I, Zhuhai Dipu Medical Technology Co., Ltd.). The right popliteal and iliac LN were resected and validated by fluorescence emission using a portable projective imaging device at an exposure time of 33 ms. The resected tissues were sliced and further treated with hematoxylin and eosin (H&E) staining for histological examination.

^{99m}Tc-ICG-HSA NPs Sentinel Lymphoscintigraphy Analysis

Sprague Dawley rats were anesthetized with an oxygen flow of 1 L/min and 2% (v/v) isoflurane and fixed to a paperboard. After injection of ^{99m}Tc-ICG-HSA NPs (11.1 MBq/50 μL) into the left footpad, dynamic lymphoscintigraphy was performed immediately for up to 1 h using a SPECT/CT scanner (Precedence 16, Philips, Netherlands). Static planar scintigraphy was performed after 1 min of scanning at 2, 4, 24, and 48-hr post-injection, respectively. SPECT acquisition was performed with 60 steps in step-and-shoot mode, 20s per step, and a matrix size of 128×128. Regions of interest (ROI) were drawn on the acquired images to obtain time-radioactivity curves. Quantitative data were expressed as gamma counts. CT and SPECT projections were reconstructed and analyzed using an EBW workstation (Philips, The Netherlands).

Comparisons of Longitudinal Planar Imaging of Rats for SLNs with ^{99m}Tc-ICG-HSA NPs and ^{99m}Tc-SC

Sprague Dawley rats were anesthetized with an oxygen flow of 1 L/min and 2% (v/v) isoflurane and fixed to a paperboard. After beside injection of ^{99m}Tc-ICG-HSA NPs or ^{99m}Tc-SC (11.1 MBq/50 μL) into the left footpad, a dynamic image acquisition was performed up to 60 min immediately after injection, and static scan images were captured for 1 min at 2 h, 4 h, 24 h, and 48 h post-injection, respectively. SPECT acquisition was performed with 60 steps in step-and-shoot mode, 20s per step, and a matrix size of 128×128. ROIs were drawn on the acquired images to obtain the time–radioactivity curves. Quantitative data were expressed as gamma counts. CT and SPECT projections were reconstructed and analyzed using an EBW workstation (Philips, The Netherlands).

Results and Discussion

Multifunctional nuclide-fluorescent probe ^{99m}Tc-ICG-HSA NPs were synthesized in two steps (Scheme 1). First, HSA and ICG were dissolved and mixed in distilled water overnight, and then put into a dialysis bag (14 kDa), which was dialyzed for

24 hr to remove free ICG, and filtered (0.22 μm) to remove the precipitated macromolecules to generate an aqueous solution of ICG-HSA NPs. The morphology of the synthesized ICG-HSA NPs using TEM is shown in Figure 1A. Using DLS to determine the hydrodynamic diameter size distribution of ICG-HSA NPs, we found that the particle size distribution was mainly concentrated at approximately 10 nm (Figure 1B). The UV-vis-NIR Abs-Em spectra of ICG and ICG-HSA NPs in PBS are shown in Figures 1C and 1D, respectively. The spectra were normalized to the maximum absorption or emission. Then, $SnCl_2$ and $^{99m}TcO4$ solutions were added to the synthesized ICG-HSA NPs solution, mixed well, placed at room temperature for 30 min, and purified by centrifugation and ultrafiltration three times. Purified ^{99m}Tc-ICG-HSA NPs were dissolved in normal saline for imaging, following the procedure outlined in Scheme 1. ^{99m}Tc-ICG-HSA NPs synthesized using this two-step method showed a high radiochemical yield and excellent stability in vitro (Figure S1).

The safety of ICG-HSA NPs in vivo was evaluated at a certified institute. For the evaluation, 40 ICR (Institute of Cancer Research) mice (17.9–19.7 g) were randomly selected and divided into two groups of 20 mice each: the normal control group and the ICG-HSA NPs administration group. On the day of administration, 10 mL/kg ICG-HSA NPs in saline (120 mg/kg) were injected into the tail vein of each mouse. The symptoms and characteristics of poisoning, the occurrence and recovery time of toxic reactions, and the death of animals in each group were recorded within 0–4 h. Body weights and deaths of the mice were recorded on days 4, 7, 10, and 14 after administration. The results showed that there was no evident abnormality in the autonomous activity, mental state, or diet of ICR mice in either group. The changes in body weight are shown in Table 1. No animal death occurred in either group during the test. The primary mouse organs in each group showed no evident pathological changes in gross anatomy (data not shown). ICG-HSA NPs did not exhibit any toxic effects after administration of twice the LD50 of free ICG (60 mg/kg), demonstrating the better biosafety of ICG-HSA NPs for clinical application.

Furthermore, the fluorescence imaging capacity of ICG-HSA NPs in SLNs was studied. The experimental mice were anesthetized with 1 L/min oxygen and 2% (v/v) isoflurane and then injected subcutaneously with 10 μg/50 μL of ICG-HSA NPs into the left footpad. Immediately after injection, dynamic fluorescence imaging was performed for 60 min. Fluorescence images were taken using an IVIS Lumina II (ex/em: 760 nm/820 nm) with an exposure time of 1 s and a field of view of 10 cm. As shown in Figure 2A, the fluorescence signal of ICG-HSA NPs was visible in the left popliteal LN (SLN) 1 min after
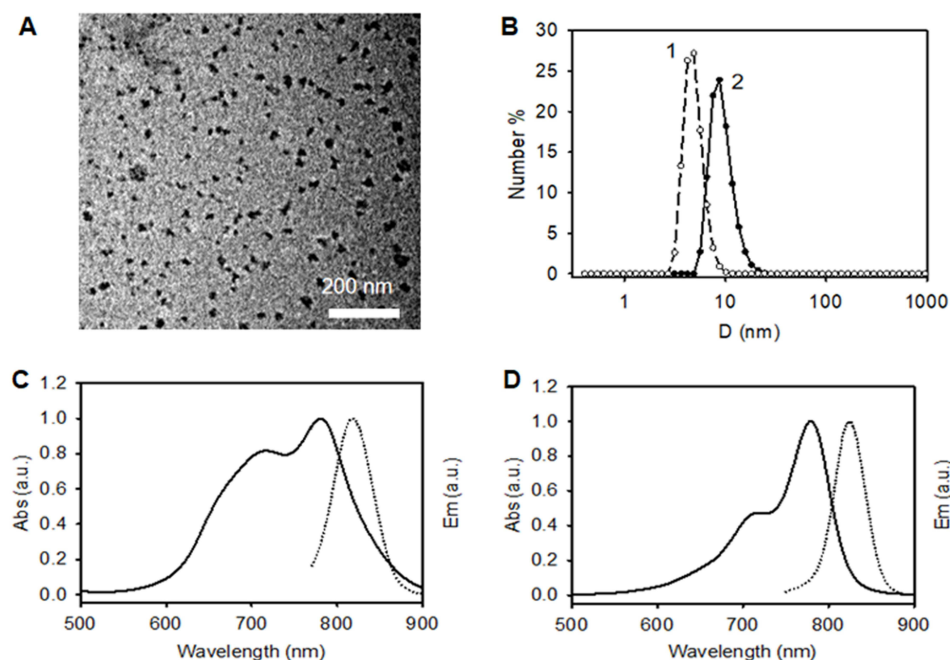

Figure 1 Characterizations of the synthesized ICG-HSA NPs. (**A**) TEM image of the synthesized ICG-HSA NPs; (**B**) Size distribution of ICG-HSA NPs measured by DLS (1 - HSA protein, 2 - ICG-HSA NPs); (**C**) Absorption and emission spectra of ICG in PBS. The spectra were normalized at the maximum absorption and emission; (**D**) Absorption and emission spectra of ICG-HSA NPs. The spectra were normalized at the maximum absorption and emission.

Table 1 Effects of ICG-HSA NPs on Body Weight of ICR Mice (n = 20, Mean ± SD)

Group	Day 0 (g)	Day 4 (g)	Day 7 (g)	Day 10 (g)	Day 14 (g)
Control group	18.7 ± 0.5	23.6 ± 2.0	26.9 ± 3.2	29.1 ± 3.9	30.6 ± 4.7
ICG-HSA NPs	18.7 ± 0.5	23.8 ± 1.7	26.7 ± 3.4	28.7 ± 4.1	30.9 ± 4.8

injection, and continuous enhancement of the fluorescence signal was observed over time. To examine SLN accumulation in the probe at the histological slice level, FITC-labeled NPs and FITC-labeled ICG-HSA NPs were subcutaneously injected into the left footpad. Two hours later, SLN was resected, fixed with 4% paraformaldehyde, dehydrated with graded alcohol, and embedded in paraffin for sectioning. One part of the SLN tissue section was stained with hematoxylin and eosin (H&E) and the other sections were stained with DAPI, which was evaluated using a fluorescence microscope with a channel of DAPI (Ex = 357/44 nm, Em = 447/60 nm) and FITC (Ex = 470/22 nm, Em = 525/50 nm) or bright field. Serial in vivo fluorescence images and hematoxylin and eosin (H&E) staining images of SLN tissue show that ICG-HSA NPs could stagnate in SLN for imaging, as illustrated in Figure 2B and C.

ICG-HSA NPs can guide SLN resection surgery using fluorescence imaging. Thirty minutes after the injection of ICG-HSA NPs solution (2 mg/mL, 50 μL) into the right footpad of Sprague Dawley rats, SLN resection surgery was performed under the guidance of a Fluorescence Imaging System device (DPM-I, Zhuhai Dipu Medical Technology Co, Ltd.). The injection site, right popliteal LN (SLN), and iliac LN (second-tier LN) were all visible by the projective imaging device, whereas the contralateral thigh muscle had no fluorescence signal (Figure 3A and B). Next, the right popliteal and iliac LN were resected and validated by fluorescence emission using a portable projective imaging device at an exposure time of 33 ms (Figure 3C). Finally, H&E staining analysis further validated the resected tissues, confirming that the fluorescence signals were LN-specific, whereas the specimen without fluorescence signals was muscle tissue (Figure 3D–F).

SLNs can be rapidly, clearly, and persistently visualized using ^{99m}Tc-ICG-HSA NPs SPECT/CT. Sprague Dawley rats were anesthetized with an oxygen flow of 1 L/min and 2% (v/v) isoflurane about half an hour before imaging, then 11.1 MBq/ 50 μL of ^{99m}Tc-ICG-HSA NPs was subcutaneously injected into the left footpad of Sprague Dawley rats. The animals were placed on the table, and dynamic lymphoscintigraphy was performed up to 1 h after injection using a SPECT/CT scanner (Precedence 16, Philips, Netherlands) (Figure S2). The camera was equipped with a low-energy, high-resolution parallel-hole
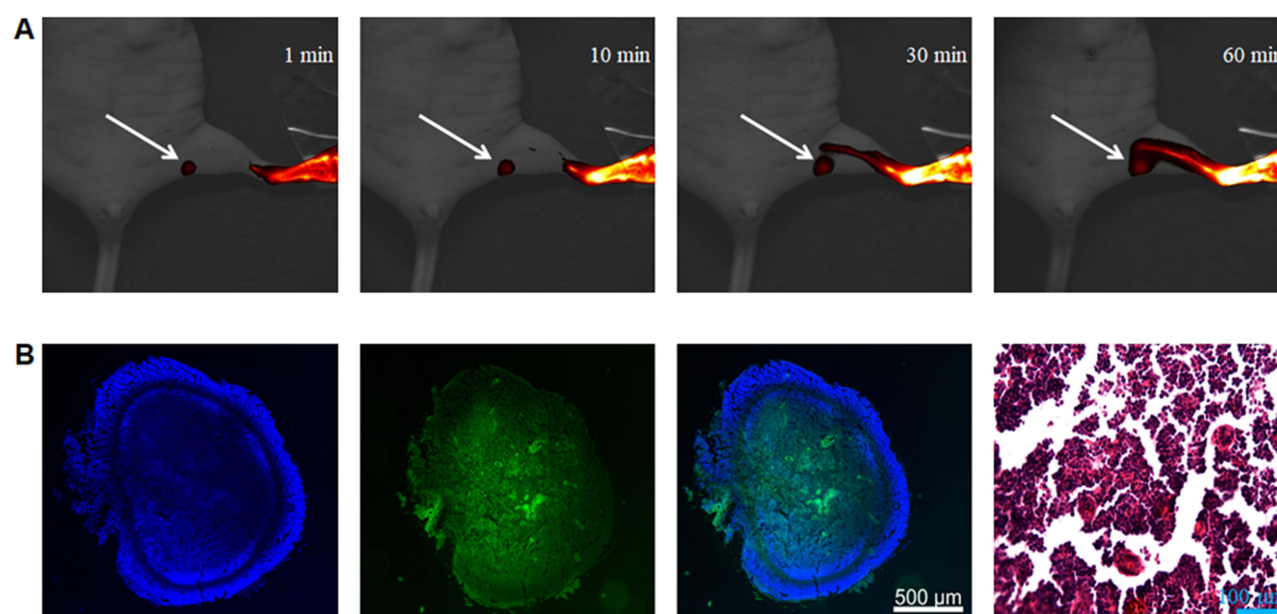

Figure 2 Dynamic fluorescence images of ICG-HSA NPs for mice SLN and slice examination of SLN. (**A**) The dynamic imaging of fluorescence from 1 minute to 60 minutes. The fluorescence signal of ICG-HSA NPs in popliteal LNs can be seen 1 min after injection, and the fluorescence signal increases continuously over time. Arrows indicate the popliteal LNs; (**B**) From left to right: DAPI, FITC-ICG-HSA NPs fluorescence, overlay images, and H&E staining of popliteal LN tissue sections (40x magnification).
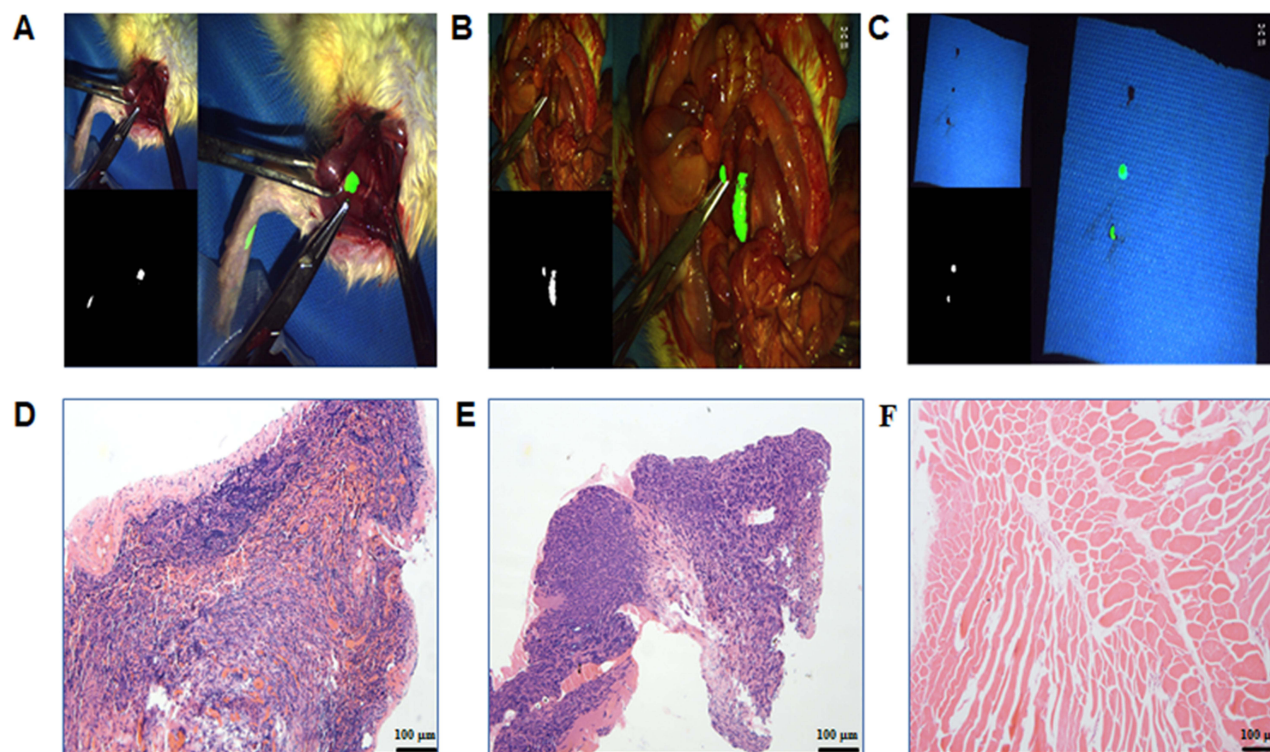
Figure 3 Fluorescence imaging of ICG-HSA NPs guiding SLN resection surgery and slice examination. (**A**) Visible light, fluorescence signals, and their real-time overlay pictures in the ICG-HSA NPs -guided SLN resection. (**B**) Visible light, fluorescence signals, and their real-time overlay during right iliac fossa lymphadenectomy guided by ICG-HSA NPs. (**C**) From top to bottom are the visible light, fluorescence signals, and their real-time overlay of the left thigh muscle, SLN, and second-tier LN. (**D–F**) H&E staining images of the SLN, second-tier LN, and left thigh muscle, respectively.

collimator and a 20% energy window centered at 140 keV. Static planar scintigraphy was obtained after 1 min of scanning at 2, 4, 24, and 48-hr post-injection. SPECT acquisition was performed with 60 steps in step-and-shoot mode, 20s per step, and a matrix size of 128×128. ROIs were drawn on the acquired images to obtain the time–radioactivity curves and the ratio of LNs to the right thigh muscle uptake value (Figure 4B). Quantitative data were expressed as gamma counts. CT and SPECT projections were reconstructed and analyzed using an EBW workstation (Philips, The Netherlands). After the injection, drainage of the SLN-left popliteal LN was observed at 5 min, with a gradual increase in uptake until it peaked at 2 h, whereas the second-tier LN-iliac LN was initially discovered at 30 min. The results of in vivo biodistribution demonstrated that [99mTc]-ICG-HSA NPs had weak radioactivity signals in the liver and spleen but strong signals in the kidney and bladder, indicating a predominant metabolic pathway via urine excretion (Figure 4A). To validate the tissue biodistribution ex vivo, 25 Sprague Dawley rats were subcutaneously injected with 7.4 MBq/50 μL [99mTc]-ICG-HSA NPs on the left footpad, and five rats were euthanized 15 min, 1, 2, 4, and 24-hr post-injection. Tissues of interest were collected, rinsed with excess blood, weighed, and counted using a γ-counter (PE, RRD2480-8010). The results are expressed as the percentage of injected dose per gram of tissue (%ID/g), which further confirms the maximum biodistribution in SLN and sub-maximum biodistribution in second-tier SLN, demonstrating the efficient application of SLN and second-tier SLN recognition by [99mTc]-ICG-HSA NPs (Figure 4C).

To further evaluate the metabolic performance and safety of the 99mTc-ICG-HSA NPs, [99mTc]-sulfur colloid (SC) was synthesized as a comparator. Similarly, 11.1 MBq/50 μL of [99mTc]-SC was also subcutaneously injected into the left rear pad, dynamic image acquisition was performed up to 60 min immediately after injection, and static scan images were captured for 1 min at 2, 4, 24, and 48 hr post-injection (Figure S3) and the biodistribution of [99mTc]-SC in the major organs and tissues of rats is shown in Figure S4. In contrast to [99mTc]-SC, [99mTc]-ICG-HSA NPs aggregated more quickly, visibly, and consistently in the SLN and second-tier LN, and a higher target-background (contralateral thigh muscle) ratio was observed between 10 and 60 min (Figure 5). Furthermore, [99mTc]-ICG-HSA NPs had a faster renal clearance rate, indicating that [99mTc]-ICG-HSA NPs may have a lower radiation exposure and are safer for further clinical trials. The radiation dosimetry in normal tissues of rats was measured using Medical Internal Radiation Dose (MIRD) method and depicted in Table S1.
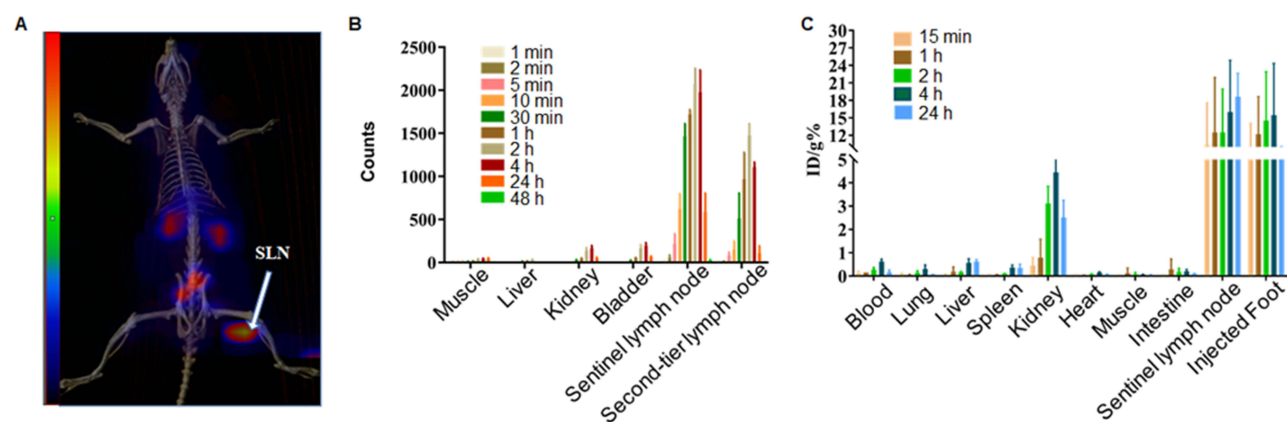
Figure 4 ^{99m}Tc-ICG-HSA NPs sentinel lymphoscintigraphy analysis. (**A**) SPECT/CT fusion image of ^{99m}Tc-ICG-HSA NPs at 1 h post plantar injection; (**B**) Radioactivity counts of ^{99m}Tc-ICG-HSA NPs in various tissues and organs in vivo at 24 h post-injection. n = 3 in each group; (**C**) Biodistribution of ^{99m}Tc-ICG-HSA NPs in various tissues and organs at 24 h post-injection. n = 3 in each group. The data are shown as mean ± SD.
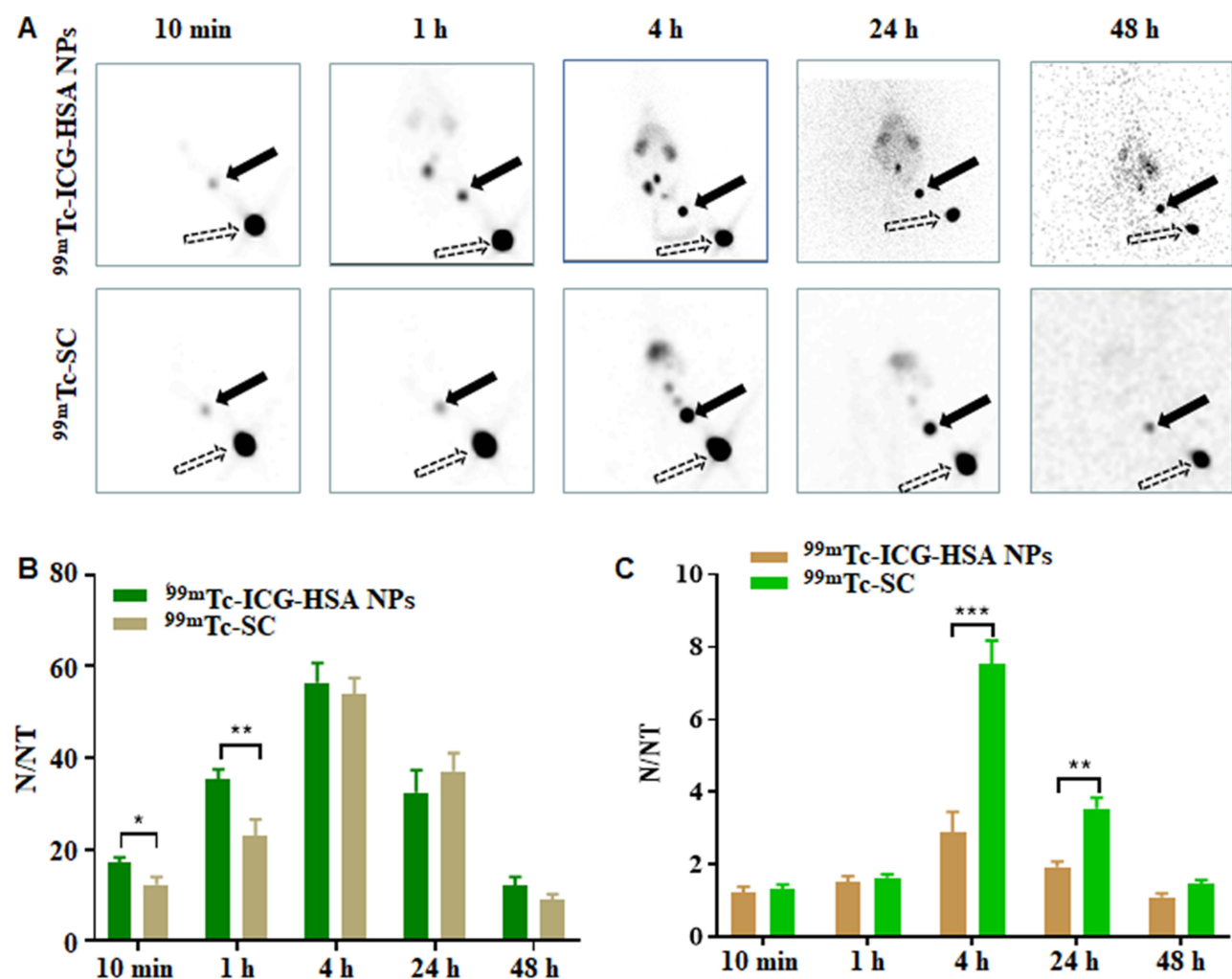

Figure 5 Comparisons of longitudinal planar imaging of rats for SLNs with ^{99m}Tc-ICG-HSA NPs and ^{99m}Tc-SC. (**A**) Planar imaging of SLNs with ^{99m}Tc-ICG-HSA NPs or 99mTc-SC. The solid arrows indicate the popliteal LNs and the dash arrows indicate the injection sites; (**B**) T/NT of SLNs to right thigh muscles in rats of ^{99m}Tc-ICG-HSA NPs and ^{99m}Tc-SC scintigraphy; (**C**) T/NT of livers to right thigh muscles in rats of ^{99m}Tc-ICG-HSA NPs and ^{99m}Tc-SC scintigraphy. N/NT = Target-to-non-target ratio. The data are shown as mean ± SD, ***P<0.001, **P<0.01, *P<0.05.

Conclusion

In summary, a dual-modality SLN imaging agent, ^{99m}Tc-ICG-HSA NPs, was successfully constructed using ^{99m}Tc-labeling NPs self-assembled by ICG and HSA. It shows reliable imaging capability for SLN by SPECT imaging and NIR fluorescence imaging and also allows for the accurate visualization of SLN and guided SLN biopsy intraoperatively. In contrast to ^{99m}Tc-SC, ^{99m}Tc-ICG-HSA NPs displayed faster SLN and second-tier LN imaging speeds and excellent renal clearance properties, suggesting that these NPs have lower radiation exposure and better safety in clinical applications. Furthermore, an acute toxicity test of the ICG-HSA NPs was performed to demonstrate their safety in vivo. ICG-HSA NPs demonstrated efficacy in NIR fluorescence imaging-guided LN surgery in rats. Taken together, ^{99m}Tc-ICG-HSA NPs can be useful as non-invasive dual-modality agents for SLN mapping.

Although the preparation was stable, the self-assembly mechanism of ^{99m}Tc-ICG-HSA have not been in-depth research. What is more, due to the human research ethics has not been approved, the pharmacokinetics and radiation dosimetry in volunteers have not been studied. In future, we will continue an in-depth study of the self-assembly mechanism and preparation method and make it into a radiolabelling kit. The study of imaging capability of SLN using SPECT imaging and NIR fluorescence imaging in cancer patients will also push ahead.

Ethics Approval

All animal experiments were performed in accordance with the guidelines and approved by the Animal Care and Use Committee of Central South University (CSU-2022-0001-0273). ICR mice and Sprague Dawley rats were purchased from the Department of Zoology, Central South University.

Acknowledgments

Disclosure

Caiting Deng and Feifei An reports a patent 2022116673082 pending to Xi'an Jiaotong University. The authors declare no other conflicts of interest in this work.

References

1. Bray F, Laversanne M, Weiderpass E, Soerjomataram I. The ever-increasing importance of cancer as a leading cause of premature death worldwide. *Cancer*. 2021;127(16):3029–3030. doi:10.1002/cncr.33587
2. Sung H, Ferlay J, Siegel RL, et al. Global cancer statistics 2020: globocan estimates of incidence and mortality worldwide for 36 cancers in 185 countries. *Ca a Cancer J Clinicians*. 2021;71(3):209–249. doi:10.3322/caac.21660
3. Gervasoni JE, Taneja C, Chung MA, Cady B. Biologic and clinical significance of lymphadenectomy. *Surgical Clinic North Am*. 2000;80 (6):1631–1673. doi:10.1016/S0039-6109(05)70253-X
4. Beek MA, Verheuvel NC, Luiten EJT, et al. Two decades of axillary management in breast cancer. *Br J Surg*. 2015;102(13):1658–1664. doi:10.1002/bjs.9955
5. Bilde A, von Buchwald C, Therkildsen MH, et al. Need for intensive histopathologic analysis to determine lymph node metastases when using sentinel node biopsy in oral cancer. *Laryngoscope*. 2008;118(3):408–414. doi:10.1097/MLG.0b013e31815d8e15
6. Christensen A, Bilde A, Therkildsen MH, et al. The prevalence of occult metastases in nonsentinel lymph nodes after step-serial sectioning and immunohistochemistry in cN0 oral squamous cell carcinoma. *Laryngoscope*. 2011;121(2):294–298. doi:10.1002/lary.21375
7. Cormier B, Diaz JP, Shih K, et al. Establishing a sentinel lymph node mapping algorithm for the treatment of early cervical cancer. *Gynecologic Oncol*. 2011;122(2):275–280. doi:10.1016/j.ygyno.2011.04.023
8. Holloway RW, Abu-Rustum NR, Backes FJ, et al. Sentinel lymph node mapping and staging in endometrial cancer: a Society of Gynecologic Oncology literature review with consensus recommendations. *Gynecologic Oncol*. 2017;146(2):405–415. doi:10.1016/j.ygyno.2017.05.027
9. Takeuchi H, Kitajima M, Kitagawa Y. Sentinel lymph node as a target of molecular diagnosis of lymphatic micrometastasis and local immunoresponse to malignant cells. *Cancer Sci*. 2008;99(3):441–450. doi:10.1111/j.1349-7006.2007.00672.x
10. Maguire A, Brogi E. Sentinel lymph nodes for breast carcinoma: an update on current practice. *Histopathology*. 2016;68(1):152–167. doi:10.1111/his.12853
11. Heerdt AS. Lymphatic mapping and sentinel lymph node biopsy for breast cancer. *JAMA Oncology*. 2018;4(3):431. doi:10.1001/jamaoncol.2017.4000

12. Cousins A, Thompson SK, Wedding AB, Thierry B. Clinical relevance of novel imaging technologies for sentinel lymph node identification and staging. *Biotechnol Adv.* 2014;32(2):269–279. doi:10.1016/j.biotechadv.2013.10.011

13. Takeuchi H, Kitagawa Y. New sentinel node mapping technologies for early gastric cancer. *Anna Surg Oncol.* 2013;20(2):522–532. doi:10.1245/s10434-012-2602-1

14. Mariani G, Moresco L, Viale G, et al. Radioguided Sentinel Lymph Node Biopsy in Breast Cancer Surgery*. *J Nucl Med.* 2001;42(8):1198–1215.

15. Fadel MG, Rauf S, Mohamed HS, et al. The use of indocyanine green and near-infrared fluorescence imaging versus blue dye in sentinel lymph node biopsy in cutaneous melanoma: a retrospective, cohort study. *Anna Surg Oncol.* 2023;30(7):4333–4340. doi:10.1245/s10434-023-13405-7

16. Rundle S, Korompelis P, Ralte A, Bewick D, Ratnavelu N. A comparison of ICG-NIR with blue dye and technetium for the detection of sentinel lymph nodes in vulvar cancer. *Eur J Surg Oncol.* 2023;49(2):481–485. doi:10.1016/j.ejso.2022.09.015

17. Goyal A, Newcombe RG, Chhabra A, Mansel RE. on behalf of the ATG. Factors affecting failed localisation and false-negative rates of sentinel node biopsy in breast cancer – results of the ALMANAC validation phase. *Breast Cancer Res Treat.* 2006;99(2):203–208. doi:10.1007/s10549-006-9192-1

18. Lee ES, Kim TS, Kim SK. Current status of optical imaging for evaluating lymph nodes and lymphatic system. *Korean J Radiol.* 2015;16(1):21–31. doi:10.3348/kjr.2015.16.1.21

19. Kitayama J, Ishigami H, Ishikawa M, et al. Hyaluronic acid is a useful tool for intraoperative sentinel node detection in gastric cancer surgery. *Surgery.* 2007;141(6):815–820. doi:10.1016/j.surg.2007.01.026

20. Emile SH, Elfeki H, Shalaby M, et al. Sensitivity and specificity of indocyanine green near-infrared fluorescence imaging in detection of metastatic lymph nodes in colorectal cancer: systematic review and meta-analysis. *J Surg Oncol.* 2017;116(6):730–740. doi:10.1002/jso.24701

21. Perissinotti A, Vidal-Sicart S, Nieweg O, Olmos RV. Melanoma and nuclear medicine. *Melanoma Manage.* 2014;1(1):57–74. doi:10.2217/mmt.14.10

22. Even-Sapir E, Lerman H, Lievshitz G, et al. Lymphoscintigraphy for sentinel node mapping using a hybrid SPECT/CT system. *J Nucl Med.* 2003;44(9):1413–1420.

23. den Toom IJ, Boeve K, Lobeek D, et al. Elective neck dissection or sentinel lymph node biopsy in early stage oral cavity cancer patients: the Dutch experience. *Cancers.* 2020;12(7):1783. doi:10.3390/cancers12071783

24. Stoeckli SJ, Huebner T, Huber GF, Broglie MA. Technique for reliable sentinel node biopsy in squamous cell carcinomas of the floor of mouth. *Head Neck.* 2016;38(9):1367–1372. doi:10.1002/hed.24440

25. Pedersen NJ, Jensen DH, Hedbäck N, et al. Staging of early lymph node metastases with the sentinel lymph node technique and predictive factors in T1/T2 oral cavity cancer: a retrospective single-center study. *Head Neck.* 2016;38(S1):E1033–E1040. doi:10.1002/hed.24153

26. Wan J, Oblak ML, Ram AS, McKenna C, Singh A, Nykamp S. Evaluating the feasibility and efficacy of a dual-modality nanoparticle contrast agent (Nanotrast-CF800) for image-guided sentinel lymph node mapping in the oral cavity of healthy dogs. *Front Vet Sci.* 2021;8:721003. doi:10.3389/fvets.2021.721003

27. Qin Z, Hoh CK, Hall DJ, Vera DR. A tri-modal molecular imaging agent for sentinel lymph node mapping. *Nucl Med Biol.* 2015;42(12):917–922. doi:10.1016/j.nucmedbio.2015.07.011

28. Deng C, Zheng M, Xin J, An F. A nanoparticle composed of totally hospital-available drugs and isotope for fluorescence/SPECT dual-modal imaging-guided photothermal therapy to inhibit tumor metastasis. *J Colloid Interface Sci.* 2023;651:384–393. doi:10.1016/j.jcis.2023.07.163

29. Jiang JX, Keating JJ, Jesus EM, et al. Optimization of the enhanced permeability and retention effect for near-infrared imaging of solid tumors with indocyanine green. *Am J Nucl Med Mol Imaging.* 2015;5(4):390–400.